Geometric-optics–integral-equation method for light scattering by nonspherical ice crystals

Ping Yang and K. N. Liou

A new geometric-optics model has been developed for the calculation of the single-scattering and polarization properties for arbitrarily oriented hexagonal ice crystals. The model uses the ray-tracing technique to solve the near field on the ice crystal surface, which is then transformed to the far field on the basis of the electromagnetic equivalence theorem. From comparisons with the results computed by the finite-difference time domain method, we show that the novel geometric-optics method can be applied to the computation of the extinction cross section and single-scattering albedo for ice crystals with size parameters along the minimum dimension as small as ~6. Overall agreement has also been obtained for the phase function when size parameters along the minimum dimension are larger than ~20. We demonstrate that the present model converges to the conventional ray-tracing method for large size parameters and produces single-scattering results close to those computed by the finite-difference time domain method for size parameters along the minimum dimension smaller than ~20. The present geometric-optics method can therefore bridge the gap between the conventional ray-tracing and the exact numerical methods that are applicable to large and small size parameters, respectively.

1. Introduction

A significant number of cloud particles in the Earth's atmosphere is ice crystals. They reflect sunlight and produce many fascinating halos and arcs in the atmosphere, and at the same time they also trap thermal infrared radiation emitted from the surface and lower atmosphere. An understanding of the radiation budget in the Earth and the atmosphere system, and hence its climate, must begin with an understanding of the scattering and absorption properties of ice crystals. The development of remote-sensing methodologies for the identification of ubiquitous visible and invisible cirrus clouds and the retrieval of their optical and microphysical properties using multispectral radiance data gathered from satellites also requires the fundamental scattering, absorption, and polarization information for ice crystals. Laboratory experiments show that the shape and size of an ice crystal are governed by temperature and supersaturation, but it generally has a basic hexagonal structure. In the atmosphere, if the ice crystal growth involves collision and coalescence, the particle shape can be extremely complex. Recent observations based on aircraft optical probes and balloonborne replicator sondes for mid-latitude cirrus clouds reveal that these clouds are largely composed of bullet rosettes, solid and hollow columns, plates, and aggregates with sizes ranging from approximately 5 to 600 μm.[1–3]

Unlike the scattering of light by spherical water droplets, which can be solved by the exact Mie theory, an exact solution for the scattering of light by hexagonal ice crystals covering all shapes and sizes does not exist in practical terms. Although several numerical methods such as the finite-difference time domain (FDTD)[4–6] and discrete dipole methods[7,8] have been developed to solve light scattering by nonspherical particles, they are usually applicable to size parameters smaller than approximately 20 in the three-dimensional (3-D) case, as discussed by Liou and Takano[9] and by Yang and Liou,[5] and the references cited therein. In the past two decades, significant research on solving light scattering by regular and complex ice crystals has been carried out by means of the geometric ray-tracing technique,[10–14] which is commonly employed to identify the optical phenomena occurring in the atmosphere. In the limit of geometric optics an incident wave may be considered as being composed of a bundle of rays that

The authors are with the Center for Atmospheric and Remote Sounding Studies, University of Utah, 809 William C. Browning Building, Salt Lake City, Utah 84112.

Received 2 November 1995; revised manuscript received 24 April 1996.

0003-6935/96/336568-17$10.00/0

strike the ice crystal and undergo reflection and refraction along a straight line. The laws of geometric optics are applicable to the scattering of light by an ice crystal if its size is much larger than the incident wavelength so that the geometric rays can be localized. In addition to the requirement of the localization principle, the conventional geometric ray-tracing technique assumes that the energy attenuated by the scatterer may be decomposed into equal extinction from diffraction and Fresnel rays. Moreover, the Fraunhofer diffraction formulation used in geometric ray tracing does not account for the vector property of the electromagnetic field and requires a Kirchhoff boundary condition, which cannot take into consideration the effect of the charges along the edge contour of the opening.

To circumvent a number of shortcomings in the geometric-optics approach, we have developed an improvement by mapping the equivalent tangential electric and magnetic (E & M) currents on the particle surface, which are obtained from geometric reflection and refraction, to the far field by means of the basic electromagnetic wave theory in two-dimensional (2-D) space.[5] In this paper we have extended the improved geometric-optics method in the 2-D case to the 3-D space, allowing arbitrary and random orientations of the ice crystals. We have also developed a new intensity mapping algorithm to economize the computer time requirement in the calculation. Section 2 presents the fundamental formulation for the geometric-optics–integral-equation hybrid method in 3-D space. The intensity mapping algorithm for practical applications is subsequently described in Section 3. In Section 4 we discuss some pertinent results and the validity of the new method with respect to the size parameter. Finally, conclusions are given in Section 5.

2. Geometric-Optics–Integral-Equation Hybrid Method in Three-Dimensional Space

We present a geometric-optics–integral-equation hybrid method (hereafter referred to as GOM2) to compute the scattering, absorption, and polarization properties of hexagonal ice crystals with arbitrary and random orientations in 3-D space. Following the conceptual approach presented by Yang and Liou[5] in the 2-D case, we apply the geometric ray-tracing technique to solve the tangential components of the electric and magnetic fields on surface S, which encloses the scatterer. These tangential components of the electromagnetic field can be used to determine the equivalent electric and magnetic currents that are then used to compute the scattered far field on the basis of the electromagnetic equivalence theorem.[15] In this theorem, the electromagnetic field detected by an observer outside the surface would be the same if the scatterer were removed and replaced by the equivalent electric and magnetic currents, given by

$$\mathbf{J} = \hat{n}_s \times \mathbf{H}, \tag{1a}$$

$$\mathbf{M} = \mathbf{E} \times \hat{n}_s, \tag{1b}$$

where electric field $\mathbf{E}$ and magnetic field $\mathbf{H}$ are the total fields that include the incident and scattered fields produced by the scatterer and $\hat{n}_s$ is the outward unit vector normal to the surface.

The mapping of the near field provided by the ray-tracing procedure to the corresponding far field is much involved in the 3-D case. In order to make the mapping algorithm practical in numerical computations, one must formulate the associated amplitude scattering matrix and various cross sections explicitly. In the 3-D case, the Hertz vectors or potentials given by the equivalent currents are as follows[16]:

$$\mathbf{j}_m(\mathbf{r}) = \iint_s \mathbf{M}(\mathbf{r}')G(\mathbf{r}, \mathbf{r}')\mathrm{d}^2\mathbf{r}', \tag{2a}$$

$$\mathbf{j}_e(\mathbf{r}) = \iint_s \mathbf{J}(\mathbf{r}')G(\mathbf{r}, \mathbf{r}')\mathrm{d}^2\mathbf{r}', \tag{2b}$$

where $G(\mathbf{r}, \mathbf{r}')$ is the Green's function in free space, which is defined by

$$G(\mathbf{r}, \mathbf{r}') = \frac{\exp(ik|\mathbf{r} - \mathbf{r}'|)}{4\pi|\mathbf{r} - \mathbf{r}'|}. \tag{2c}$$

In Eqs. (2), $\mathbf{r}$ is the position vector of the observation point, $\mathbf{r}'$ is the position vector of the source point, k is the wave number, and $i = \sqrt{-1}$. The induced electric field by the Hertz vectors can be written in the form

$$\mathbf{E}^s(\mathbf{r}) = -\nabla \times \mathbf{j}_m(\mathbf{r}) + \frac{i}{k} \nabla \times \nabla \times \mathbf{j}_e(\mathbf{r}). \tag{3}$$

For the radiation zone or far-field region, i.e., $kr \to \infty$, Eq. (3) reduces to

$$\mathbf{E}^s(\mathbf{r})|_{kr\to\infty} = \frac{\exp(ikr)}{-ikr} \frac{k^2}{4\pi} \hat{r} \times \iint_s \{\hat{n}_s \times \mathbf{E}(\mathbf{r}') - \hat{r} \times [\hat{n}_s \times \mathbf{H}(\mathbf{r}')]\} \exp(-ik\hat{r} \cdot \mathbf{r}')\mathrm{d}^2\mathbf{r}', \tag{4}$$

where $\hat{r} = \mathbf{r}/r$ is the scattering direction. It is evident that the far field can be obtained exactly if the tangential components of the electric and magnetic fields on surface S are precisely known. A method known as the modified Kirchhoff approximation (MKA) has been developed by Muinonen[13] to solve the scattering by nonspherical particles based on Eq. (4) in which the surface field is the pure scattered field. In the MKA, a constant extinction efficiency of 2 is assumed and one can approximate the strong forward-scattering maximum by using the Fraunhofer diffraction formula for a circular aperture of the equivalent area of the particle projection.

As pointed out in Section 1 and in Ref. 5, the conventional geometric ray-tracing technique (referred to as GOM1) has a number of shortcomings in computing the scattered field. By the performance of the exact mapping from the near field to the far field, the only approximation in the present geometric-

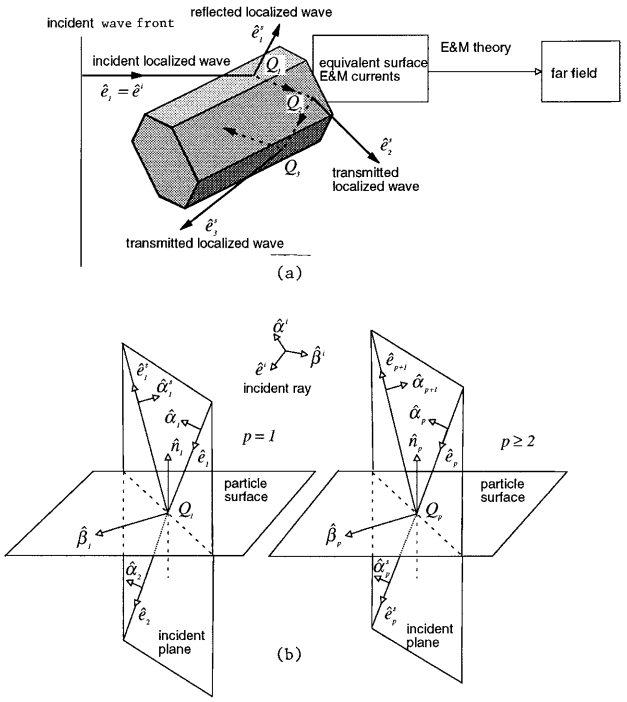

Fig. 1. (a) Conceptual diagram of the geometric-optics–integral-equation method. (b) The polarization configuration of the localized waves for external reflection ($p = 1$) and two refraction and internal reflections ($p \geq 2$). The directions of various unit vectors are defined.

optics–integral-equation method is confined to the calculation of the surface field by means of geometric ray tracing. The concept of the present method for a 3-D ice crystal is demonstrated in Fig. 1(a). When the particle is large, the incident wave front can be divided into a number of localized waves or geometric rays. Each localized wave, after interacting with the particle, leads to various orders of outgoing (or scattered) rays produced by the Fresnel reflection and refraction on the particle surface. The direction of the incoming rays that are observed at the incident points Q_p ($p = 1, 2, 3, \ldots$) are specified by unit vectors $\hat{e}_p$, and the directions of the outgoing rays are denoted by $\hat{e}_p{}^s$, in which subscript p denotes the order of incidence for the incoming ray at point Q_p ($p = 1$, external reflection; $p = 2$, two refraction, etc.). From the 3-D geometry and Snell's law, it can be proved for rays inside the particle that

$$\hat{e}_2 = N_r^{-1}\{\hat{e}_1 - (\hat{e}_1 \cdot \hat{n}_1)\hat{n}_1 - [N_r^2 - 1 + (\hat{e}_1 \cdot \hat{n}_1)^2]^{1/2}\hat{n}_1\}, \tag{5a}$$

$$\hat{e}_p = \hat{e}_{p-1} - 2(\hat{e}_{p-1} \cdot \hat{n}_{p-1})\hat{n}_{p-1}, \quad p = 3, 4, 5, \ldots. \tag{5b}$$

For rays outside the particle (with superscript s) we have

$$\hat{e}_1{}^s = \hat{e}_1 - 2(\hat{e}_1 \cdot \hat{n}_1)\hat{n}_1, \tag{5c}$$

$$\hat{e}_p{}^s = N_r\{\hat{e}_p - (\hat{e}_p \cdot \hat{n}_p)\hat{n}_p - [N_r^{-2} - 1 + (\hat{e}_p \cdot \hat{n}_p)^2]^{1/2}\hat{n}_p\}, \quad p = 2, 3, 4, \ldots, \tag{5d}$$

where we define the initial incident direction $\hat{e}_1 = \hat{e}^i$. Unit vectors $\hat{n}_p$ denote the normal directions at incident points Q_p on the particle surface that faces the incoming rays, and N_r is the real part of the adjusted refractive index. When absorption is involved, the energy transport and phase propagation of a localized ray differ. In order to approximate the inhomogeneous wave based on the homogeneous condition so that geometric ray tracing can be performed, we have introduced a set of refractive indices based on the optical principle to compute both the ray direction and Fresnel coefficients.[5] In Eq. (5d), when $N_r^{-2} + (\hat{e}_p \cdot \hat{n}_p)^2 < 1$, total reflection takes place and the corresponding transmitted ray does not occur in this case. Equations (5a)–(5d) constitute a self-closing algorithm to trace the propagation of the localized waves for a given incident ray. However, in addition to the propagating directions, the polarization configuration is also required to describe the complete behavior of the localized waves. In the 3-D case, the polarization configuration of a localized wave will be changed after the wave undergoes reflection and refraction. As shown in Fig. 1(b), let the polarization configuration of the incident wave be specified by unit vectors $\hat{\alpha}^i$ and $\hat{\beta}^i$ that satisfy

$$\hat{e}^i = \hat{\beta}^i \times \hat{\alpha}^i. \tag{6}$$

The incident plane at point Q_p is the one that contains unit vectors $\hat{e}_p{}^s$, $\hat{e}_p$, $\hat{n}_p$, and $\hat{e}_{p+1}$. Let $\hat{\beta}_p$ be the unit vectors perpendicular to the incident plane at point Q_p. It follows that

$$\hat{\beta}_p = (\hat{n}_p \times \hat{e}_p)[1 - (\hat{e}_p \cdot \hat{n}_p)^2]^{-1/2}, \quad p = 1, 2, 3, \ldots. \tag{7}$$

When $\hat{e}_p \cdot \hat{n}_p = -1$, the incident plane cannot be specified uniquely. In this case we choose $\hat{\beta}_p = \hat{\beta}_{p-1}$ (note that $\hat{\beta}_0 = \hat{\beta}^i$). After $\hat{\beta}_p$ is determined, the polarization of the electric field that is parallel to the incident plane can be specified for the outgoing and incoming rays by the unit vectors at each incident point, given by

$$\hat{\alpha}_p{}^s = \hat{e}_p{}^s \times \hat{\beta}_p, \quad p = 1, 2, 3, \ldots, \tag{8a}$$

$$\hat{\alpha}_p = \hat{e}_p \times \hat{\beta}_p, \quad p = 1, 2, 3, \ldots. \tag{8b}$$

Because the transverse wave condition is assumed for the localized waves in geometric optics, the polarized electric field of the outgoing rays at position $\mathbf{r}$ along the ray path can be expressed by

$$\mathbf{E}_p{}^s(\mathbf{r}) = \hat{\alpha}_p{}^s E_{p,\alpha}{}^s(\mathbf{r}) + \hat{\beta}_p E_{p,\beta}{}^s(\mathbf{r}). \tag{9}$$

Similarly, the polarized electric field associated with the ray propagating along $\hat{e}_p$ inside the particle is

$$\mathbf{E}_p(\mathbf{r}) = \hat{\alpha}_p E_{p,\alpha}(\mathbf{r}) + \hat{\beta}_p E_{p,\beta}(\mathbf{r}). \tag{10}$$

Let the amplitude of the initial incident wave be given by

$$\mathbf{A} = \begin{bmatrix} A_\alpha \\ A_\beta \end{bmatrix} = \hat{\alpha}^i A_\alpha + \hat{\beta}^i A_\beta. \tag{11}$$

Then the components of the electric field in Eqs. (9) and (10) can be written as

$$\mathbf{E}_1(\mathbf{r}) = \begin{bmatrix} E_{1,\alpha}(\mathbf{r}) \\ E_{1,\beta}(\mathbf{r}) \end{bmatrix} = \mathbf{U}_1\mathbf{A}\exp[ik(\hat{e}_1\cdot\mathbf{r})], \tag{12a}$$

$$\mathbf{E}_1{}^s(\mathbf{r}) = \begin{bmatrix} E_{1,\alpha}{}^s(\mathbf{r}) \\ E_{1\beta}{}^s(\mathbf{r}) \end{bmatrix} = \mathbf{U}_1{}^s\mathbf{A}\exp\{ik[\hat{e}_1\cdot\mathbf{r}_{Q_1} + \hat{e}_1{}^s\cdot(\mathbf{r}-\mathbf{r}_{Q_1})]\}, \tag{12b}$$

$$\mathbf{E}_p(\mathbf{r}) = \begin{bmatrix} E_{p,\alpha}(\mathbf{r}) \\ E_{p,\beta}(\mathbf{r}) \end{bmatrix} = \mathbf{U}_p\mathbf{A}\exp\left\{ik\left[\hat{e}_1\cdot\mathbf{r}_{Q_1} + N\sum_{j=1}^{P-2} d_j + N\hat{e}_p\cdot(\mathbf{r}-\mathbf{r}_{Q_{p-1}})\right]\right\},\ p = 2, 3, 4, \ldots, \tag{12c}$$

$$\mathbf{E}_p{}^s(\mathbf{r}) = \begin{bmatrix} E_{p,\alpha}{}^s(\mathbf{r}) \\ E_{p,\beta}{}^s(\mathbf{r}) \end{bmatrix} = \mathbf{U}_p{}^s\mathbf{A}\exp\left\{ik\left[\hat{e}_1\cdot\mathbf{r}_{Q_1} + N\sum_{j=1}^{P-1} d_j + \hat{e}_p{}^s\cdot(\mathbf{r}-\mathbf{r}_{Q_p})\right]\right\},\quad p = 2, 3, 4, \ldots, \tag{12d}$$

where position vector $\mathbf{r}$ is along the path of the ray, $N = N_r + iN_i$ is the adjusted refractive index,[5] $\mathbf{r}_{Q_p}$ is the position vector at incident point Q_p, and $d_j = |\mathbf{r}_{Q_{j+1}} - \mathbf{r}_{Q_j}|$ is the distance between two successive incident points.

In Eq. (12c), the second term in the exponent is equal to zero for $p = 2$. Using the Fresnel reflection and refraction coefficients, we obtain

$$\mathbf{U}_1 = \Lambda_1, \tag{13a}$$

$$\mathbf{U}_2 = \mathbf{T}_1\mathbf{U}_1, \tag{13b}$$

$$\mathbf{U}_p = \mathbf{R}_{p-1}\Lambda_{p-1}\mathbf{U}_{p-1},\quad p = 3, 4, 5, \ldots, \tag{13c}$$

$$\mathbf{U}_1{}^s = \mathbf{R}_1\mathbf{U}_1, \tag{13d}$$

$$\mathbf{U}_p{}^s = \mathbf{T}_p\Lambda_p\mathbf{U}_p,\quad p = 2, 3, 4, \ldots, \tag{13e}$$

where

$$\mathbf{R}_p = \begin{bmatrix} R_{p,\alpha} & 0 \\ 0 & R_{p,\beta} \end{bmatrix},\quad p = 1, 2, 3, \ldots, \tag{13f}$$

$$\mathbf{T}_p = \begin{bmatrix} T_{p,\alpha} & 0 \\ 0 & T_{p,\beta} \end{bmatrix},\quad p = 1, 2, 3, \ldots, \tag{13g}$$

in which $(R_{p,\alpha}, R_{p,\beta})$ and $(T_{p,\alpha}, T_{p,\beta})$ are the Fresnel reflection and refraction coefficients at point Q_p for the two polarization configurations, respectively, and Λ_p $(p = 1, 2, 3, \ldots)$ are the matrices associated with the coordinate transform, defined in Appendix A. In what follows, all the matrices associated with the projection and the rotation of coordinate systems are defined in Appendix A for simplicity of the presentation.

The surface for the integral in Eq. (4) is arbitrary as long as it encloses the scattering particle. If an ice crystal shape of great complexity is involved, such as bullet rosettes and aggregates, the surface can be defined as a cubic box so that the computation of the equivalent currents can be conducted on a regularly shaped surface. If the surface is selected to be the particle surface, this surface, after illumination, can be divided into the illuminated and shadowed sides. The surface electric field can be obtained by the ray-tracing technique as follows:

$$\mathbf{E}(\mathbf{r}) = \begin{cases} \mathbf{E}_a(\mathbf{r}) + \mathbf{E}_b(\mathbf{r}),\ \mathbf{r}\in\text{illuminated side} \\ \mathbf{E}_b(\mathbf{r}),\ \mathbf{r}\in\text{shadowed side} \end{cases}, \tag{14a}$$

where

$$\mathbf{E}_a(\mathbf{r}) = \mathbf{E}_1(\mathbf{r}) + \mathbf{E}_1{}^s(\mathbf{r}), \tag{14b}$$

$$\mathbf{E}_b(\mathbf{r}) = \sum_{\gamma}\sum_{p=2}^{\infty}\mathbf{E}_p{}^s(\mathbf{r}). \tag{14c}$$

In Eq. (14c) the summation is made for all incident rays denoted by γ. Because the total field can be regarded as a linear superposition of the incident field and the induced (or scattered) field, it is clear from Eq. (14a) that the induced field on the shadowed side is $\mathbf{E}_b(\mathbf{r}) - \mathbf{E}^i(\mathbf{r})$, within which the part of $-\mathbf{E}^i(\mathbf{r})$ is polarized in the opposite direction but with the same magnitude as the incident wave and will produce a strong forward-scattering peak that corresponds to the diffraction maximum in the conventional geometric-optics method, as pointed out in our previous study[5]. From Eq. (4) the $\mathbf{H}$ field is required to map the near field to the far field. Although only the $\mathbf{E}$ field is given by the ray-tracing scheme, we can obtain the $\mathbf{H}$ field because the transverse electromagnetic wave condition is implied in ray tracing, that is, for a given outgoing ray we have

$$\mathbf{H}_p{}^s(\mathbf{r}) = \hat{e}_p{}^s\times\mathbf{E}_p{}^s(\mathbf{r}),\quad \text{for } \mathbf{r}\in\text{outside the particle.} \tag{15}$$

In GOM2, when we applied the ray-tracing technique to obtain the surface field, the area elements from which the externally reflected and transmitted localized waves make a contribution to the surface waves must be properly accounted for. Let the cross section of the incident localized wave be $\Delta\sigma_0$. Then for external reflection, the area on the particle surface at which the localized wave makes a contribution is given by

$$\Delta\tilde{\sigma}_1{}^s = -\Delta\sigma_0(\hat{n}_1\cdot\hat{e}^i)^{-1}. \tag{16a}$$

For the transmitted rays, the area is given by

$$\Delta\tilde{\sigma}_p{}^s = -\Delta\sigma_0(n_1\cdot\hat{e}_2)[(\hat{n}_1\cdot\hat{e}^i)(\hat{n}_p\cdot\hat{e}_p)]^{-1},\quad \text{for } p = 2, 3, 4, \ldots. \tag{16b}$$

In numerical computations, we find that the radius of the cross section of a ray should be of the order of k^{-1} so that the phase change over the ray cross section is not significant and the phase interference of the localized waves can be properly accounted for by using the phase information at the centers of the rays. In addition, because the phase variation over the ray cross section can be neglected, the numerical results are not sensitive to the shape of the ray cross sections. For this reason we use the

circular cross section for the current ray-tracing studies. After we determined the surface **E** and **H** fields by ray tracing, the equivalent electromagnetic currents can be defined and subsequently mapped to obtain the far field.

As we pointed out above, the strong forward-scattering peak in GOM2, which corresponds to the Fraunhofer diffraction in GOM1, is inherently produced by the scattered surface wave on the shadowed side of the particle surface. However, this peak is from the mapping of $\mathbf{E}_a(r)$ in Eq. (14a) on the illuminated side because the near field involved in the mapping is the total field rather than the scattered field. The scattered energy associated with the mapping of $\mathbf{E}_a(\mathbf{r})$ is coherent, and the distribution of this part of the scattered energy oscillates greatly with the scattering angle. In the 3-D case, we find that small errors in solving the phase of the near field for the mapping of $\mathbf{E}_a(\mathbf{r})$ can be significantly amplified. To avoid potential errors in numerical computations, we map $\mathbf{E}_a(\mathbf{r})$ and $\mathbf{E}_b(\mathbf{r})$ in Eq. (14a) separately to the far field. Let us first consider the mapping of $\mathbf{E}_b(\mathbf{r})$. Following Eq. (4), we find that the scattered field associated with this part of the energy is

$$\mathbf{E}_b{}^s(\mathbf{r})|_{kr\to\infty} = \frac{\exp(ikr)}{-ikr}\frac{k^2}{4\pi}\hat{r}\times\iint_s\left\{\sum_\gamma\sum_{p=2}^{\infty}\{\hat{n}_{s,p}\times\mathbf{E}_p{}^s(\mathbf{r}') - \hat{r}\times[\hat{n}_{s,p}\times\mathbf{H}_p{}^s(\mathbf{r}')]\}\exp(-ik\hat{r}\cdot\mathbf{r}')\mathrm{d}^2r', \tag{17}$$

where $\hat{n}_{s,p}$ is a local outward-pointing unit vector on the particle surface at which the outgoing ray emerges. It is evident from Eq. (17) that the scattered far field, $\mathbf{E}_b{}^s(\mathbf{r})$, is a transverse wave with respect to the scattering direction, and it can be expressed in terms of the components parallel and perpendicular to the scattering plane determined by incident and scattering directions as follows:

$$\mathbf{E}_b{}^s(\mathbf{r}) = \hat{\alpha}^s E_{b,\alpha}{}^s(\mathbf{r}) + \hat{\beta}^s E_{b,\beta}{}^s(\mathbf{r}), \tag{18}$$

where $\hat{\alpha}^s$ and $\hat{\beta}^s$ are the unit vectors parallel and perpendicular, respectively, to the scattering plane, which satisfy

$$\hat{r} = \hat{\beta}^s\times\hat{\alpha}^s. \tag{19}$$

For scattering along the exact forward and backward directions with respect to the incident ray, the scattering plane cannot be determined uniquely. In this case, we select the plane on which the incident polarization configuration is specified as the scattering plane. Next, we define two unit vectors $\hat{\mu}_p$ and $\hat{v}_p$ on the particle surface locally that satisfy

$$\hat{\mu}_p\times\hat{v}_p = \hat{n}_{s,p}. \tag{20}$$

From Eqs. (17)–(20) we obtain the following equation after carrying out some algebraic manipulations:

$$\mathbf{E}_b{}^s(\mathbf{r}) = \begin{bmatrix} E_{b,\alpha}{}^s(\mathbf{r}) \\ E_{b,\beta}{}^s(\mathbf{r}) \end{bmatrix} = \frac{\exp(ikr)}{-ikr}\mathbf{S}_b{}^i\mathbf{A}, \tag{21a}$$

$$\mathbf{S}_b{}^i(\hat{r}) = \frac{k^2}{4\pi}\sum_\gamma\sum_{p=2}^{\infty}\Delta\tilde{\sigma}_p{}^s[\mathbf{J}\mathbf{K}_p\mathbf{J}\mathbf{Y}_p{}^s + \mathbf{K}_p\mathbf{J}\mathbf{Y}_p{}^s\mathbf{J}]\mathbf{U}_p{}^s \times\exp\left[ik\left(\hat{e}^i\cdot\mathbf{r}_{Q_1} + N\sum_{j=1}^{p-1}\mathrm{d}_j - \hat{r}\cdot\mathbf{r}_{Q_p}\right)\right], \tag{21b}$$

where $\mathbf{K}_p$, $\mathbf{Y}_p{}^s$, and $\mathbf{J}$ are matrices associated with the projection and rotation of coordinate systems defined in Appendix A. The introduction of matrix $\mathbf{Y}_p{}^s$ in Eq. (21b) is to economize the numerical computation, because the polarization of outgoing rays can be specified on the particle surface in terms of the four unit vectors, $\hat{\alpha}_p{}^s$, $\hat{\beta}_p$, $\hat{\mu}_p$, and $\hat{v}_p$, rather than in reference to scattering directions. The number of particle faces is smaller than the number of scattering directions at which the scattered field must be solved. Thus, the storage requirement in computation can be largely reduced. In Eq. (21a), **A** is the amplitude of the incident field expressed in the incident coordinate system specified by $\hat{\alpha}^i$ and $\hat{\beta}^i$, denoted in Eq. (11). In Eq. (21b) we have performed summation over the contributions from the individual rays denoted by γ. This equation requires the mapping of the near field to the far field for each ray.

For simplicity in numerical computations, we rewrite this equation as follows:

$$\mathbf{S}_b{}^i(\hat{r}) = \frac{k^2}{4\pi}\sum_n\Delta S_n\left\{\sum_\gamma\sum_{p=2}^{\infty}(\Delta\tilde{\sigma}_p{}^s/\Delta S_n) \times[\mathbf{J}\mathbf{K}_p\mathbf{J}\mathbf{Y}_p{}^s + \mathbf{K}_p\mathbf{J}\mathbf{Y}_p{}^s\mathbf{J}]\mathbf{U}_p{}^s \times\exp\left[ik\left(\hat{e}^i\cdot\mathbf{r}_{Q_1} + N\sum_{j=1}^{p-1}\mathrm{d}_j - \hat{r}\cdot\mathbf{r}_{Q_p}\right)\right]\right\}, \tag{21c}$$

where ΔS_n is a small area element that is divided on the mapping surface such that it is much smaller than the locally planar face of the mapping surface in which the edge effect of the mapping surface is negligible. In addition, the phase change over the area element is insignificant so that an average phase factor can be used for the mapping of the near field on the area element. Subject to the aforementioned conditions, all rays may be traced to obtain the near field on the mapping surface and then transform the total near field to the far field. In order to obtain the amplitude scattering matrix, we need to transform **A** to the scattering plane. After the transformation, we obtain the amplitude scattering matrix, $\mathbf{S}_b(\hat{r})$, associated with the mapping of $\mathbf{E}_b(\mathbf{r})$ as follows:

$$\mathbf{S}_b(\hat{r}) = \mathbf{S}_b{}^i(\hat{r})\Gamma^i, \tag{22}$$

where rotational matrix Γ^i is defined in Appendix A and $\mathbf{S}_b{}^i(\hat{r})$ is given in Eq. (21b).

For the mapping involving $\mathbf{E}_a(\mathbf{r})$ on the illuminated side of the particle surface, an analytic expression

can be obtained, which not only ensures the numerical accuracy but also reduces the CPU time in comparison with the preceding algorithm in the mapping of $\mathbf{E}_b(\mathbf{r})$. Only four planar faces on the particle surface can be illuminated once the orientation of a hexagonal ice crystal is specified. Thus, the index γ, which denotes different incident rays, can be grouped into four domains: $\tilde{\gamma}_j$, $j = 1$–4. For $\gamma \in \tilde{\gamma}_j$, the incident rays impinge on face #j. For a given illuminated face, the field amplitudes are the same for incident rays but their phases differ. Similarly, different externally reflected rays for a given face have the same field amplitudes but with different phases. Thus, instead of carrying out the discrete summation over rays, we can integrate the contribution from the incident wave and external reflection over a planar face. Using the expressions given by Eqs. (12a) and (12b) for the incident and externally reflected waves, respectively, we obtain the scattering matrix from the mapping of $\mathbf{E}_a(\mathbf{r})$ as follows:

$$\mathbf{S}_a(\hat{r}) = \sum_{j=1}^{4} D_j \mathbf{S}_{a,j}(\hat{r}), \tag{23a}$$

where

$$\mathbf{S}_{a,j}(\hat{r}) = \frac{k^2}{4\pi}[\mathbf{J}\mathbf{K}_1\mathbf{J}(\mathbf{Y}_1^s\mathbf{U}_1^s + \mathbf{Y}_1\mathbf{U}_1) + \mathbf{K}_1\mathbf{J} \times (\mathbf{Y}_1^s\mathbf{J}\mathbf{U}_1^s + \mathbf{Y}_1\mathbf{J}\mathbf{U}_1)]\mathbf{\Gamma}^i, \quad \gamma \in \tilde{\gamma}_j, \tag{23b}$$

and D_j is the integration over face #j defined by

$$D_j = \int_{\#j}\int_{\text{face}} \exp[ik(\hat{e}^i - \hat{r})\cdot\mathbf{r}']\mathrm{d}^2r'. \tag{24}$$

Analytical expressions for D_j ($j = 1$–4) can be derived. Evidently, Eq. (23b) requires only the incident and scattering geometries and does not involve ray-tracing calculations.

The total scattering matrix from the mapping of the near field to the far field can be written in the form

$$\mathbf{S}(\hat{r}) = \begin{bmatrix} S_2 & S_3 \\ S_4 & S_1 \end{bmatrix} = \mathbf{S}_a(\hat{r}) + \mathbf{S}_b(\hat{r}). \tag{25}$$

Using Eq. (25), we can define the corresponding Stokes phase matrix in a straightforward manner. The mean extinction cross section can be obtained by using the forward scattering on the basis of the optical theorem[17] given by

$$\bar{\sigma}_e = (\sigma_{e,/\!/} + \sigma_{e,\perp})/2 = \frac{2\pi}{k^2}\,\mathrm{Re}[S_1(\hat{e}^i) + S_2(\hat{e}^i)], \tag{26}$$

where $\sigma_{e,/\!/}$ and $\sigma_{e,\perp}$ are the extinction cross sections for the two polarized configurations. The mean value $\bar{\sigma}_e$ is independent of the specification of the scattering plane, however. The absorption cross section can be expressed in terms of an integral equation as follows[18]:

$$\sigma_a = \frac{k\varepsilon_i}{|\mathbf{E}^i|^2}\int\int_v\int \mathbf{E}(\mathbf{r})\cdot\mathbf{E}^*(\mathbf{r})\mathrm{d}^3\mathbf{r}, \tag{27}$$

where the asterisk denotes a complex conjugate and the domain of integration is the volume enclosed by the particle surface. In the limit of geometric optics and applying the ray-tracing procedure described above, we can prove that the absorption cross section is given by

$$\begin{aligned}\bar{\sigma}_a &= \frac{1}{2}(\sigma_{a,/\!/} + \sigma_{a,\perp}) \\ &= \frac{1}{2}\sum_{\gamma}\sum_{p=2}^{\infty}\Delta\sigma_0(\hat{n}_1\cdot\hat{e}^i)^{-1}(\hat{n}_1\cdot\hat{e}_2)N_r \\ &\quad\times\exp\left(-2kN_i\sum_{j=1}^{p-1}\mathrm{d}_j\right)[1 - \exp(-2kN_i d_p)] \\ &\quad\times[|U_{p,11}|^2 + |U_{p,12}|^2 + |U_{p,21}|^2 + |U_{p,22}|^2],\end{aligned} \tag{28}$$

where terms $U_{p,ij}$, $i = 1$–2, and $j = 1$–2, are the elements of matrix $\mathbf{U}_p$ defined in Eq. (13).

3. Intensity Mapping Algorithm for GOM2

An intensity mapping algorithm has been developed to economize the computational requirement for GOM2. We write the scattered field from the mapping of $\mathbf{E}_a(\mathbf{r})$ given in Eq. (14b) in two parts, denoted by $\mathbf{E}_i^s(\mathbf{r})$ and $\mathbf{E}_r^s(\mathbf{r})$; the former is associated with the incident localized waves on the illuminated particle surface and the latter is associated with external reflection. We find by means of numerical experiments that the phase denoted in Eq. (21b) for $\mathbf{E}_b^s(\mathbf{r})$ varies greatly for different transmitted localized waves when size parameters are larger than approximately 20–30, and that the effects of the phase interference are washed out in the computation of the phase matrix, particularly for randomly oriented ice crystals. However, sensitivity of the phase effect has been noted in computing $\mathbf{E}_i^s(\mathbf{r})$ because this part of the scattered energy is always coherent regardless of the particle size and produces a strong peak in the forward-scattering direction, corresponding to Fraunhofer diffraction in the conventional method. Coherence is also noted in determining $\mathbf{E}_r^s(\mathbf{r})$ from each planar face on the particle surface, evidenced from the inclusion of integral D_i given by Eq. (24) in the calculation of the far field contributed by external reflection. Except in the research of Cai and Liou,[10] the phase interference of externally reflected rays has not been considered in all the previous geometric-optics models with which we assume that the phase interference of external reflection is destructive and may be smoothed out when ice crystals are large. For a large particle, because D_i decreases significantly when the scattering angle increases, GOM1 will overestimate the contribution of external reflection for the scattered energy at large scattering angles. The phase interference in computing $\mathbf{E}_r^s(\mathbf{r})$,

however, can be accounted for approximately by considering the ray spreading, which is discussed in Appendix B. Because the scattered energy associated with $\mathbf{E}_r{}^s(\mathbf{r})$ accounts for only a few percent of the total scattered energy, the approximate treatment of the phase effect for the external reflection is adequate for numerical calculations when ray spreading is included. Thus, intensity mapping can be carried out for computing the intensity and polarization pattern for the scattered energy associated with both $\mathbf{E}_r{}^s(\mathbf{r})$ and $\mathbf{E}_b{}^s(\mathbf{r})$.

In what follows, we should first present the equivalent counterpart of Eq. (4), which involves only the electric field and is convenient for conducting the intensity mapping. Based on the vector algorithm, it can be proved that the following relationships hold for two arbitrary vectors $\mathbf{P}$ and $\mathbf{Q}$ and a scalar function ϕ:

$$\int\int_v\int (\mathbf{Q}\cdot\nabla\times\nabla\times\mathbf{P}-\mathbf{P}\cdot\nabla\times\nabla\times\mathbf{Q})\mathrm{d}v$$
$$=\int\int_v\int (\mathbf{P}\cdot\nabla^2\mathbf{Q}-\mathbf{Q}\cdot\nabla^2\mathbf{P})\mathrm{d}v+\oiint_s \hat{n}_s\cdot(\mathbf{Q}\nabla\cdot\mathbf{P}$$
$$-\mathbf{P}\nabla\cdot\mathbf{Q})\mathrm{d}s, \tag{29}$$

$$\int\int_v\int (\phi\nabla^2\mathbf{P}-\mathbf{P}\nabla^2\phi)\mathrm{d}v$$
$$=\oiint_s\left(\phi\frac{\partial\mathbf{P}}{\partial n_s}-\mathbf{P}\frac{\partial\phi}{\partial n_s}\right)\mathrm{d}s, \tag{30}$$

where S is an arbitrary surface that encloses the volume domain V. By applying Eqs. (29) and (30) to obtain the mapping equations, we let

$$\mathbf{P}=\mathbf{a}\cdot\bar{\bar{G}},\qquad \mathbf{Q}=\mathbf{E},\qquad \phi=G, \tag{31}$$

where $\mathbf{a}$ is an arbitrary constant vector, G is the Green's function, and $\bar{\bar{G}}$ is the dyadic Green's function[19] given by

$$\bar{\bar{\mathbf{G}}}(\mathbf{r},\mathbf{r}')=\left(\bar{\bar{\mathbf{I}}}+\frac{1}{k^2}\nabla_r\nabla_r\right)G(\mathbf{r},\mathbf{r}'), \tag{32}$$

where $\bar{\bar{\mathbf{I}}}$ is a unit dyad. As shown in Fig. 2, volume domain V is selected to be the region outside S and S_0 but bounded by S_∞, where S_0 encloses the source that generates the incident wave (active source), S encloses the scatterer (passive source), and S_∞ denotes a surface infinitely far away. The distance between S_0 and S must be large enough so that the impact of the scattered field on the source inside S_0 can be neglected.

Using Eqs. (29)–(31), we obtain the electric field

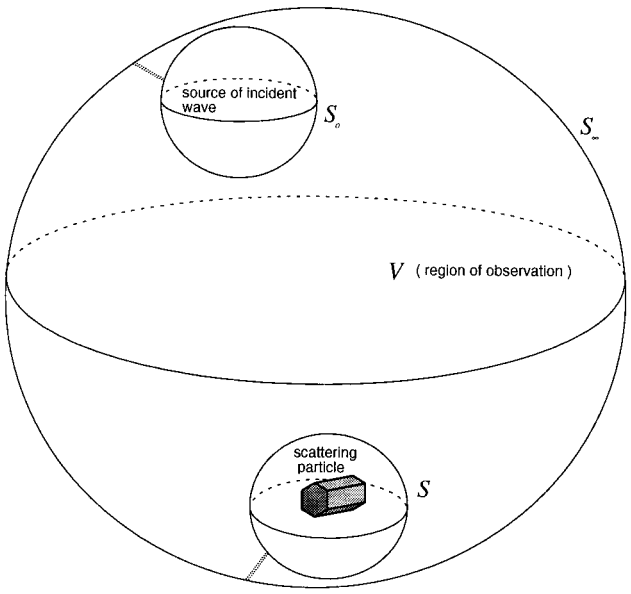

Fig. 2. Conceptual geometry for the active and passive sources in light scattering by a dielectric particle.

observed inside the region of V as follows:

$$\mathbf{E}(\mathbf{r})=\frac{1}{k^2}\nabla\times\nabla\times\left[\oiint_{S_\infty}+\oiint_S+\oiint_{S_0}\right]\left[\mathbf{E}(\mathbf{r}')\frac{\partial G(\mathbf{r},\mathbf{r}')}{\partial n_s}\right.$$
$$\left.-G(\mathbf{r},\mathbf{r}')\frac{\partial\mathbf{E}(\mathbf{r}')}{\partial n_s}\right]\mathrm{d}^2\mathbf{r}',\quad \mathbf{r}\in V, \tag{33}$$

where the integral over S_0 is associated with the incident or initial wave. There will be no contribution from the integral over S_∞ if we apply the following Sommerfeld radiation condition[19]:

$$\lim_{r\to\infty} r[\nabla\times\bar{\bar{\mathbf{G}}}-ik\hat{r}\times\bar{\bar{\mathbf{G}}}]=0. \tag{34}$$

It follows that the scattered or induced field caused by the presence of a scatterer is

$$\mathbf{E}^s(\mathbf{r})=\frac{1}{k^2}\nabla\times\nabla\times\oiint_s\left[\mathbf{E}(\mathbf{r}')\frac{\partial G(\mathbf{r},\mathbf{r}')}{\partial n_s}\right.$$
$$\left.-G(\mathbf{r},\mathbf{r}')\frac{\partial\mathbf{E}(\mathbf{r}')}{\partial n_s}\right]\mathrm{d}^2\mathbf{r}',\quad \mathbf{r}\in V. \tag{35}$$

Wolf[20] derived a similar expression. However, the surface in his expression is the particle surface that is approached from inside and is not proper for the present application. We note that instead of using macroelectrodynamics, one can use molecular optics[21] to obtain Wolf's expression. For the far-field

region, Eq. (35) reduces to

$$\mathbf{E}^s(\mathbf{r})|_{kr\to\infty} = \frac{\exp(ikr)}{-ikr}\frac{k^2}{4\pi}\hat{r}\times\left\{\hat{r}\times\oiint_s\left[\hat{n}_s\cdot\hat{r}\mathbf{E}(\mathbf{r}') + \frac{1}{ik}\frac{\partial\mathbf{E}(\mathbf{r}')}{\partial n_s}\right]\exp(-ik\hat{r}\cdot\mathbf{r}')\mathrm{d}^2\mathbf{r}'\right\}. \quad (36)$$

In deriving Eq. (36) from Eq. (35), we used the following relationship:

$$\nabla_r G(\mathbf{r},\mathbf{r}') = -\nabla_{r'}G(\mathbf{r},\mathbf{r}'). \quad (37)$$

Equation (36) is equivalent to Eq. (4), but it does not contain the **H** field and is also simpler for numerical computations.

To solve for the second term in the integrand, consider the following relationship for a localized wave that propagates along the direction specified by unit vector $\hat{e}_p{}^s$ in the form

$$\frac{1}{ik}\frac{\partial\mathbf{E}_p{}^s(\mathbf{r}')}{\partial n_s} = (\hat{e}_p{}^s\cdot\hat{n}_s)\mathbf{E}_p{}^s(\mathbf{r}'). \quad (38)$$

By using Eqs. (36) and (38), the amplitude scattering matrix $\mathbf{S}^i$, associated with $\mathbf{E}_i{}^s(\mathbf{r})$, can be written in the form

$$\mathbf{S}^i(\hat{r}) = \sum_{j=1}^{4} D_j\tilde{\mathbf{S}}_j{}^i(\hat{r}), \quad (39)$$

where D_j (j = 1–4) are the same as in Eq. (39) and $\tilde{\mathbf{S}}_j{}^i$ are given by

$$\tilde{\mathbf{S}}_j{}^i(\hat{r}) = -\frac{k^2}{4\pi}(\hat{n}_{s,1}\cdot\hat{r} + \hat{n}_{s,1}\cdot\hat{e}_1)\Pi_1\mathbf{U}_1\Gamma^i, \quad \gamma\in\tilde{\gamma}_j, \quad (40)$$

where Π_1 is defined in Appendix A. With the scattering matrix defined by Eq. (39), the phase matrix, P^i, associated with $\mathbf{S}^i(\hat{r})$ can be defined and computed. The scattering cross section contributed from this part of the scattered energy can be obtained by performing the following integration:

$$\sigma_s{}^i = \frac{1}{2k^2}\int_0^{2\pi}\int_0^{\pi}[|S_1{}^i|^2 + |S_2{}^i|^2 + |S_3{}^i|^2 + |S_4{}^i|^2]\sin\theta\mathrm{d}\theta\mathrm{d}\varphi, \quad (41)$$

where θ and φ are the zenith and azimuthal angles, respectively.

For the mapping of externally reflected and transmitted rays, the phase interference can be accounted for approximately by considering the ray spreading when the characteristic size parameters are larger than approximately 20–30. Thus, we map the near-field intensity to obtain the far-field intensity for the externally reflected and transmitted rays with the inclusion of ray spreading. Based on numerical experimentation, the interference among the three parts of scattered energy $\mathbf{E}_i{}^s$, $\mathbf{E}_r{}^s$, and $\mathbf{E}_b{}^s$ can be neglected when the characteristic size parameters are larger than approximately 20–30. Thus, we use

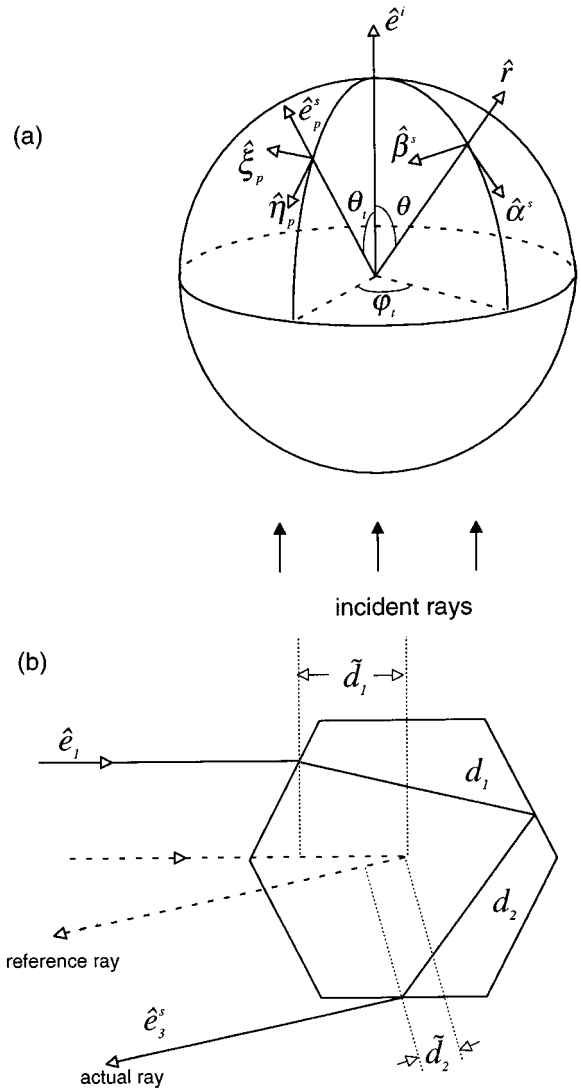

Fig. 3. (a) Large sphere on which the near field is mapped to the far field by the intensity mapping algorithm. The ice particle is located at the center. A number of unit vectors are also defined. (b) Phase delay of a ray inside an ice crystal.

a large sphere centered on the particle for mapping the external reflection and transmitted rays, as shown in Fig. 3(a). The sphere is so large that the scatterer can be regarded as a geometric point. On the sphere, the observed outgoing rays propagate along the direction normal to the sphere, namely, $\hat{e}_p{}^s = \hat{n}_{s,p}$. Moreover, the phase of the rays on the sphere can be proved to be $k(\rho + \delta_p)$, where ρ is the radius of the sphere, and δ_p is the phase delay of the ray with respect to a reference ray that passes through the center of the particle given by

$$\delta_p = N\sum_{j=1}^{p-1}\mathrm{d}_j - (\tilde{d}_1 + \tilde{d}_2), \quad (42)$$

where $\tilde{d}_1$ and $\tilde{d}_2$ are defined in Fig. 3(b). Using the notations defined in the preceding discussion, we can write the electric field associated with the outgoing

ray on the sphere as follows:

$$\mathbf{E}_p^s = \begin{bmatrix} E_{p,\eta}^s \\ E_{p,\xi}^s \end{bmatrix} = \hat{\eta}_p E_{p,\eta}^s + \hat{\xi}_p E_{p,\xi}^s = \tilde{\mathbf{Y}}_p^s \mathbf{U}_p^s \mathbf{A} \exp[ik(\rho + \delta_p)], \tag{43}$$

where $\tilde{\mathbf{Y}}_p^s$ is a rotational matrix defined in Appendix A, $\mathbf{U}_p^s$ is defined in Eqs. (13d) and (13e), and $\mathbf{A}$ is given in Eq. (11), which can be written as follows:

$$\mathbf{A} = \begin{bmatrix} A_\alpha \\ A_\beta \end{bmatrix} = \tilde{\Gamma}_p^i \Gamma_p^s \mathbf{A}^s, \tag{44a}$$

where $\tilde{\Gamma}_p^i$ and Γ_p^s are the transformation matrices defined in Appendix A and $\mathbf{A}^s$ is the amplitude of the decomposed incident field with respect to the scattering plane determined by $\hat{e}^i$ and $\hat{r}$ in the form

$$\mathbf{A}^s = \begin{bmatrix} A_\alpha^s \\ A_\beta^s \end{bmatrix} = (\hat{e}^i \times \hat{\beta}^s) A_\alpha^s + \hat{\beta}^s A_\beta^s. \tag{44b}$$

Substituting Eq. (43) into the basic far-field equation, we obtain the contribution of each individual outgoing ray to the far field as follows:

$$\mathbf{E}_p^s|_{kr\to\infty} = \frac{\exp(ikr)}{-ikr} \mathbf{S}_p^s \mathbf{A}^s, \tag{45a}$$

where the superscript s denotes that the scattered (externally reflected or transmitted) ray and the amplitude scattering matrix are

$$\mathbf{S}_p^s = \frac{k^2}{4\pi} q \exp(ik\zeta)(1 + \hat{r} \cdot \hat{e}_p^s) \tilde{\mathbf{K}}_p \tilde{\mathbf{S}}_p^s \Gamma_p^s, \tag{45b}$$

where

$$\zeta = \rho(1 - \hat{r} \cdot \hat{e}_p^s) + \delta_p, \tag{45c}$$

$$q = \iint_{\text{ray cross section}} \exp(-ik\hat{r} \cdot \mathbf{r}') \mathrm{d}^2 r' = \Delta\sigma_p^s \frac{2J_1\{k(\Delta\sigma_p^s/\pi)^{1/2} \sin[\cos^{-1}(\hat{e}_p^s \cdot \hat{r})]\}}{k(\Delta\sigma_p^s/\pi)^{1/2} \sin[\cos^{-1}(\hat{e}_p^s \cdot \hat{r})]}, \tag{45d}$$

$\Delta\sigma_p^s$ is the area of the cross section for the pth order outgoing ray, J_1 is the first-order Bessel function, and

$$\tilde{\mathbf{S}}_p^s = \tilde{\mathbf{Y}}_p^s \mathbf{U}_p^s \tilde{\Gamma}_p^i \tag{45e}$$

is the amplitude scattering matrix computed from the conventional GOM1 method. In this manner the amplitude scattering matrix for GOM2 is related to that for GOM1. Consequently, we can improve the phase matrix results computed by GOM1. For the computational purpose and in consideration of the spherical geometry depicted in Fig. 3(a), we rewrite Eq. (45b) in the form

$$\mathbf{S}_p^s = -\frac{k^2}{4\pi} \exp(ik\zeta[\mathbf{f} \cdot \tilde{\mathbf{S}}_p^s + \mathbf{g} \cdot \tilde{\mathbf{S}}_p^s \mathbf{J}], \tag{46a}$$

where

$$\mathbf{f} = h \cos\varphi_t \Xi, \qquad \mathbf{g} = h \sin\varphi_t \Xi, \tag{46b}$$

$$h = \Delta\sigma_p^s (1 + \cos\Theta) J_1(\chi)/\chi,$$

$$\cos\Theta = \cos\theta \cos\theta_t + \sin\theta \sin\theta_t \cos\varphi_t, \tag{46c}$$

$$\chi = k(\Delta\sigma_p^s/\pi)^{1/2} \sin\Theta. \tag{46d}$$

In Eq. (46b), Ξ is the directional cosine matrix defined in Appendix A. For ice crystals randomly oriented in 3-D space, the Stokes phase matrix is given by

$$\mathbf{P} = \begin{bmatrix} P_{11} & P_{12} & 0 & 0 \\ P_{12} & P_{22} & 0 & 0 \\ 0 & 0 & P_{33} & -P_{43} \\ 0 & 0 & P_{43} & P_{44} \end{bmatrix}. \tag{47}$$

The phase matrix associated with the amplitude scattering matrix given in Eq. (45b) can then be written as

$$\mathbf{P}^s = (1 - f_\delta)\pi \tilde{\mathbf{P}}^s + 4\pi f_\delta \mathbf{P}^\delta, \tag{48}$$

where f_δ is the ratio of the delta-transmitted energy[11] to the externally reflected and transmitted energy. In Eq. (48) the first term is the component of the phase matrix produced by the outgoing transmitted and externally reflected rays in which the spreading effect is accounted for, whereas the second term is the component of the phase matrix associated with the delta transmission in which $P_{43}^\delta = 0$. Note that the normalized phase matrix computed from the conventional geometric-optics method for the scattered energy of external reflection and transmission can be written as follows:

$$\mathbf{P}^c(\theta_t) = (1 - f_\delta)\tilde{\mathbf{P}}^c(\theta_t) + 2f_\delta \mathbf{I}\delta(1 - \cos\theta_t), \tag{49}$$

where δ is the Dirac delta function and $\mathbf{I}$ is a 4 by 4 unit matrix. From Eqs. (45) and the definition of the Stokes phase matrix, the six independent elements in $\tilde{\mathbf{P}}^s$ and $\mathbf{P}^\delta$ can be derived explicitly in terms of phase matrix $\mathbf{P}^c$. For example, the phase function components are given by

$$\tilde{P}_{11}^s(\theta) = 2\int_0^\pi \{[F_{11}(\theta, \theta_t) + G_{11}(\theta, \theta_t)]\tilde{\mathbf{P}}_{11}^c(\theta_t) + [F_{12}(\theta, \theta_t) + G_{12}(\theta, \theta_t)]\tilde{\mathbf{P}}_{12}^c(\theta_t)\} \sin\theta_t \mathrm{d}\theta_t, \tag{50a}$$

$$P_{11}^\delta(\theta) = F_{11}(\theta, 0) + G_{11}(\theta, 0). \tag{50b}$$

Terms F_{11}, F_{12}, G_{11}, and G_{12} are given by

$$X_{11} = c(\langle x_1^2 \rangle + \langle x_2^2 \rangle + \langle x_3^2 \rangle + \langle x_4^2 \rangle)/2, \tag{51a}$$

$$X_{12} = c(\langle x_2^2 \rangle - \langle x_3^2 \rangle + \langle x_4^2 \rangle - \langle x_1^2 \rangle)/2, \tag{51b}$$

where X stands for F and G, and x stands for f and g in which f_i and g_i are the elements of the matrices defined by Eq. (46b) and c is a normalization factor

related to the energy conservation before and after spreading is considered. The fences denote the average over φ_t. For example,

$$\langle x_1^2 \rangle = \frac{1}{2\pi} \int_0^{2\pi} x_1^2(\theta, \theta_t, \varphi_t) \mathrm{d}\varphi_t. \tag{52}$$

It is clear that the mapped phase matrix can be obtained by carrying out a convolution integral involving the phase matrix determined from GOM1. Because $F_{ij}(\theta, \theta_t)$ and $G_{ij}(\theta, \theta_t)$ (ij = 11, 12) are independent of the ray-tracing procedure, the algorithm is much more efficient than the field-mapping method developed in Section 2. To understand the physical meaning of $F_{ij}(\theta, \theta_t)$ and $G_{ij}(\theta, \theta_t)$, we use Eqs. (48), (49) and (50) to rewrite the phase function as follows:

$$P_{11}^s(\theta) = 2\pi \int_0^{\pi} \{[F_{11}(\theta, \theta_t) + G_{11}(\theta, \theta_t)] P_{11}^c(\theta_t) + [F_{12}(\theta, \theta_t) + G_{12}(\theta, \theta_t)] P_{12}^c(\theta_t)) \sin \theta_t \mathrm{d}\theta_t. \tag{53}$$

In the integrand, the first term denotes the scattered energy in direction θ_t obtained by GOM1 that is spread to direction θ. The second term is due to the polarization configuration when the spreading is included. Thus, $[F_{11}(\theta, \theta_t) + G_{11}(\theta, \theta_t)]$ actually determines the angular distribution of the spreading, whereas the polarization effect of the spreading is provided by $[F_{12}(\theta, \theta_t) + G_{12}(\theta, \theta_t)]$. It should be noted that the discontinuous scattered energy caused by the delta transmission in GOM1[11] no longer exists when the ray-spreading effect is accounted for.

Because the phase interference of outgoing rays can be neglected, the scattering cross section, σ_s^s, which is associated with the transmitted and externally reflected energies, can be obtained from the conventional ray-tracing algorithm by summing the energies carried by individual outgoing rays. Thus, the normalized total phase matrix is given by

$$\mathbf{P} = \frac{\sigma_s^i}{\sigma_s^i + \sigma_s^s} \mathbf{P}^i + \frac{\sigma_s^s}{\sigma_s^i + \sigma_s^s} \mathbf{P}^s, \tag{54}$$

where $\mathbf{P}^i$ is the phase matrix we computed by using scattering matrix $\mathbf{S}^i$ as given by Eq. (39), whereas $\mathbf{P}^s$ is given by Eq. (48).

4. Numerical Results and Discussions

The applicability and accuracy of the geometric-optics method have been investigated by Liou and Hansen[22] for spheres, by Takano and Tanaka[23] for infinite cylinders, and more recently by Macke *et al.*[24] and Lock[25] for spheroids. The exact solutions are available for these shapes having smooth surfaces. However, verification of the ray optics method for nonspherical particles with sharp discontinuities on the surface such as hexagons has not been carried out. In what follows, the applicability of the ray optics method is investigated by comparisons with the FDTD method for light scattering by solid and hollow columns, plates, and bullet rosettes, which commonly occur in cirrus clouds. The FDTD method has been applied to light scattering by hexagonal particles in the 2-D case in our previous study,[5] and it was recently extended to the 3-D case.[6] It should be pointed out that two hexagonal ice crystals with different sizes and aspect ratios but having the same equivalent-sphere radius can produce substantial differences in the scattering configurations. The approximation we made by using the equivalent-volume sphere is better than that made when we used the equivalent-surface sphere for small particles, but the reverse is true for large particles. This is because the surface wave associated with diffraction is most significant when the particle is large, whereas for a small particle the dipole moment that is proportional to the particle volume dominates the scattered field. For the reasons stated above, defining the size parameter in terms of the radius of an equivalent sphere for nonspherical ice crystals is not physically appropriate.

Figure 4 shows the extinction efficiency values computed by GOM1, GOM2, and the FDTD method for a randomly oriented hexagonal ice column (L/a = 6) at λ = 0.55 and 3.7 μm, where L is the length and a is the semiwidth of an ice crystal. Also shown is the single-scattering albedo at λ = 3.7 μm. The computation with the FDTD method is applicable to size parameters (along the maximum dimension) smaller than ~30 because of the numerical limitation and computer time requirement. The extinction efficiency computed by GOM1 is independent of the particle size and is equal to 2; this is a result of the assumption that the extinction energies associated with diffraction and Fresnel rays are the same as those intercepted by the particle cross section projected along the incident direction. The extinction efficiency computed by GOM2 displays oscillating patterns as a function of size parameter. GOM1 and GOM2 converge for very large size parameters at which the vector property of electromagnetic fields associated with the light beam and the phase interference between the outgoing rays become less important. It is evident that when kL = 20, the GOM2 and FDTD method results converge for both wavelengths. Thus, in computing the extinction efficiency, GOM2 can be applied with acceptable accuracy when the size parameter is larger than approximately 20. For λ = 3.7 μm, at which the absorption of ice is noticeable, the GOM1 and GOM2 methods converge for size parameters larger than approximately kL = 200 (or ka = 33). Absorption of the refracted rays inside the ice crystal greatly reduces the difference between GOM1 and GOM2.

In GOM2, two parts of the near-field electromagnetic field are mapped to the far field separately in the 3-D case, leading to scattering matrices $S_a(\hat{r})$ and $S_b(\hat{r})$. The computation of $S_a(\hat{r})$ is efficient in practice because analytic expressions can be derived. However, the tedious ray-tracing calculations are required to solve $S_b(\hat{r})$. The typical computer time required by GOM2 in the computation of the phase

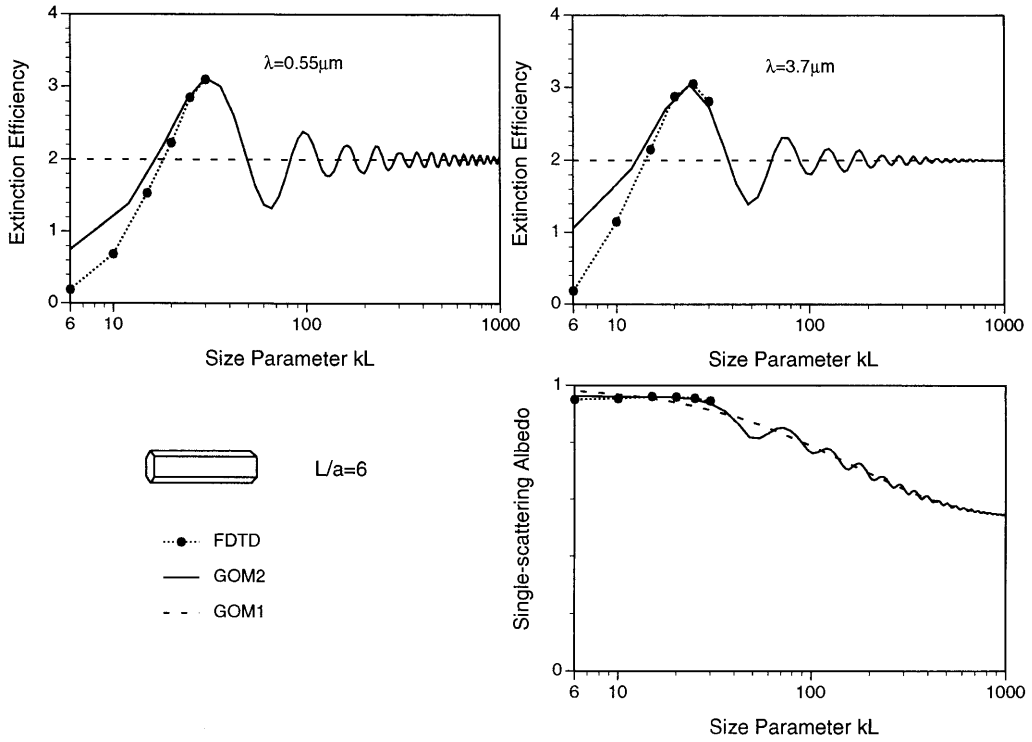

Fig. 4. Extinction efficiency computed by GOM1 and GOM2 at $\lambda = 0.55$ and 3.7 μm. The refractive indices of ice at these wavelengths are $m = 1.311 + i3.11 \times 10^{-9}$ and $m = 1.4005 + i7.1967 \times 10^{-3}$. Also shown are the single-scattering albedos computed by GOM1 and GOM2 at $\lambda = 3.7$ μm. The exact FDTD results for size parameters less than 30 are also presented.

matrix for size parameter $ka = 20$ with $L/a = 1$ is ~4 h on a Silicon Graphics Indigo 2 workstation. As we stated in the preceding discussion, the radius of the cross section of the rays in GOM2 should be of the order of k^{-1} so that the required computer time is proportional to $(ka)^2$ if the aspect ratio is fixed. We find that the field-mapping algorithm of GOM2 presented in Section 2 is not a practical method for computing the phase matrix for ice crystals with size parameters larger than approximately 40–50, although it can be effectively used to calculate the extinction and absorption cross sections by employing the Monte Carlo method in terms of the random shooting technique for incident rays.

To economize the computational requirement of GOM2, in Section 3 we developed an intensity mapping algorithm for ice crystals with size parameters larger than approximately 20–30 for the calculation of the phase matrix. To verify the feasibility of the intensity mapping algorithm, we compare the phase functions computed by the field-mapping and intensity mapping algorithms for randomly oriented ice crystals with $L/a = 1$ for three size parameters at two wavelengths, as illustrated in Fig. 5. Close agreement between the two methods is shown. The variation in the phase function computed by the intensity mapping algorithm is smoother, particularly in the scattering angle region between 15 and 80°, because this algorithm does not consider the phase interference between various transmitted rays and between the diffracted and externally reflected rays. The agreement between the two methods appears to be better for larger size parameters. Absorption does not play a significant role in the comparison. Similar results are obtained for other phase matrix elements. Significant differences of the two methods for size parameters smaller than ~20 are noted, although the results are not presented here. From a number of numerical experimentations, we estimate that the intensity mapping algorithm can be reliably applied to ice crystals whose minimum characteristic size parameters are larger than ~20. The intensity mapping algorithm is a computationally efficient approximation, and its required computer time is independent of the particle size parameter associated with Fresnel rays that are used in the conventional geometric ray-tracing method.

With the intensity-mapping algorithm, it becomes practical in numerical computations to map the near field on the particle surface to the far field for large size parameters. Figure 6 shows the phase function and the degree of linear polarization computed by the conventional (GOM1) and improved (GOM2) geometric-optics methods at the 0.55- and 3.7-μm wavelengths for a size parameter of 200. At this size parameter, the two methods essentially converge. A better agreement is noted for the phase function at $\lambda = 3.7$ μm because of absorption of the refracted rays inside the particle. In the scattering angle region from 10 to 20°, the

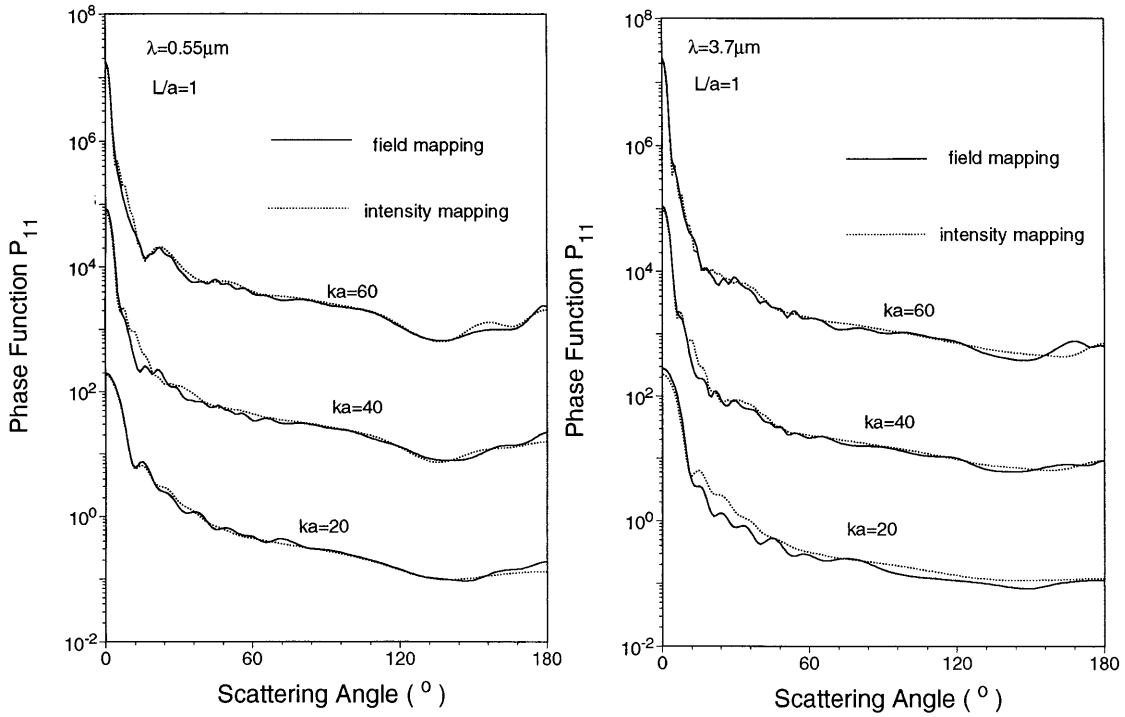

Fig. 5. Phase functions computed by the intensity and field mapping algorithms for randomly oriented plate crystals for three size parameters at two wavelengths. The vertical scale is applied to $ka = 20$; for $ka = 40$ and 60, this scale should be decreased by 10^2 and 10^3, respectively.

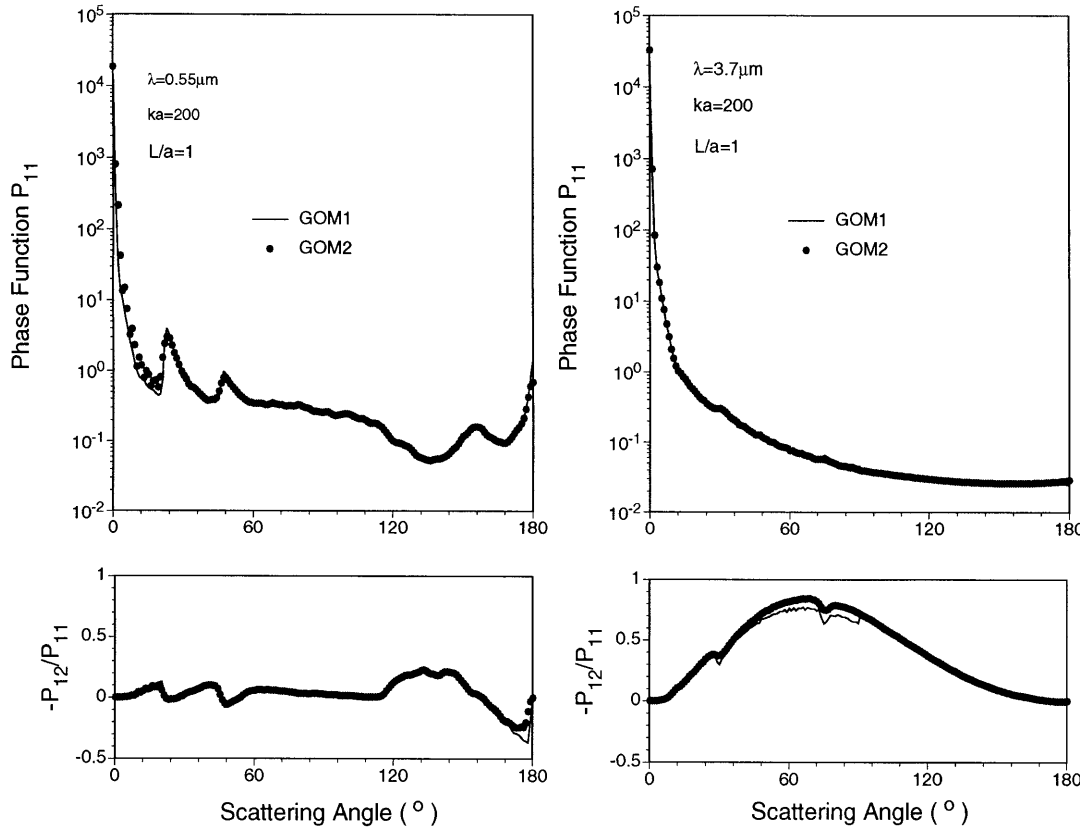

Fig. 6. Comparison of the phase function and degree of linear polarization computed by GOM1 and GOM2 for the size parameter of 200 at the 0.55-μm and 3.7-μm wavelengths.

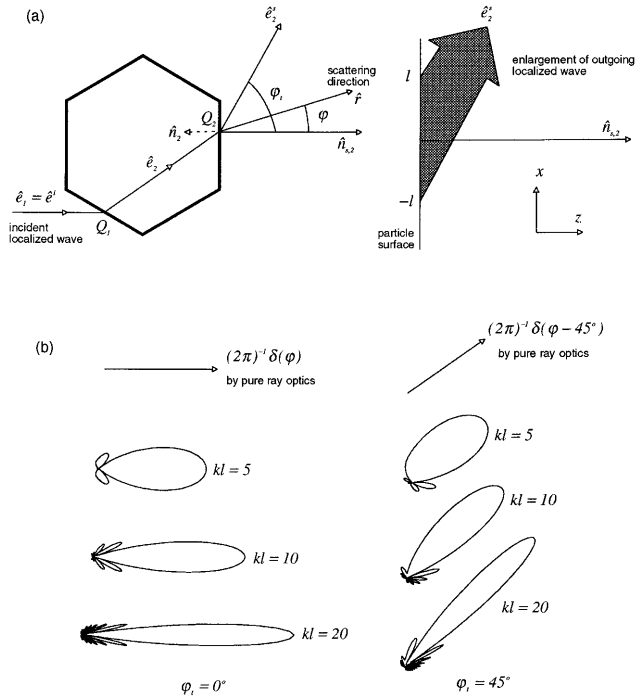

Fig. 7. (a) Geometry for an outgoing ray in 2-D space. (b) Angular distribution of the far-field intensity produced by the ray for different size parameters and scattering angles.

phase function computed by GOM2 at $\lambda = 0.55$ μm reveals some small fluctuations related to the side-scattering lobes caused by the spreading effect illustrated in Fig. 7. Backscattering computed by GOM2 at the 0.55-μm wavelength is slightly smaller than that computed by GOM1. Slight deviations of the polarization pattern are also noted in some scattering angle regions. Note that the distributions of the scattered energy and polarization for the scattering angles larger than 60° are independent of particle size in GOM1.

We studied the variation in phase function and the degree of linear polarization as functions of size parameter by using GOM2 for three size parameters increased by a factor of 3 successively, as shown in Fig. 8. The phase function at the 0.55-μm wavelength for $ka = 20$ shows ripple structures instead of halo peaks in the 10–80° scattering angle region. These ripple structures are produced from diffraction and phase interference. For $ka = 60$, a single halo peak at 22° can be seen. When $ka = 180$, the characteristic scattering features predicted by GOM2 are essentially the same as those computed by GOM1, except in the region of 5–20°, where small fluctuations occur. For these three size parameters, variations in the phase function at $\lambda = 0.55$ μm are mainly in the forward directions, the region near the 22° halo angle, and in the backscattering directions. In contrast, for $\lambda = 3.7$ μm, the phase function varies greatly for different size parameters

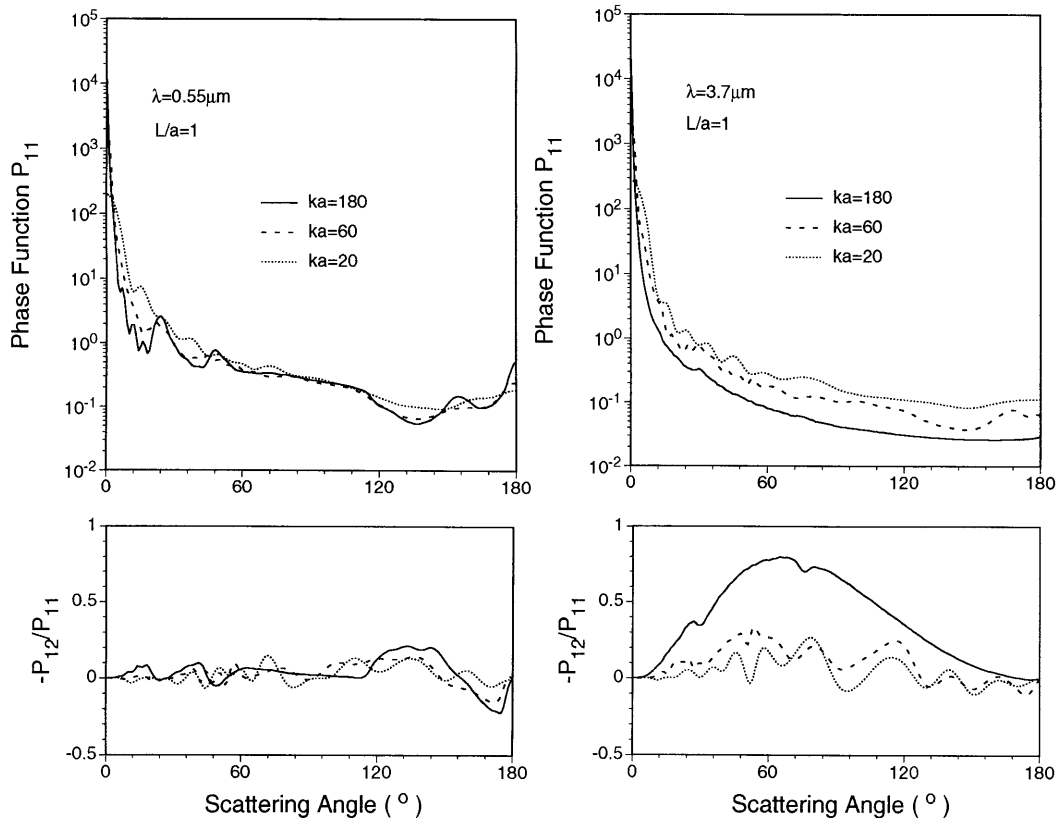

Fig. 8. Phase functions and degrees of linear polarization for three size parameters and two wavelengths computed by GOM2.

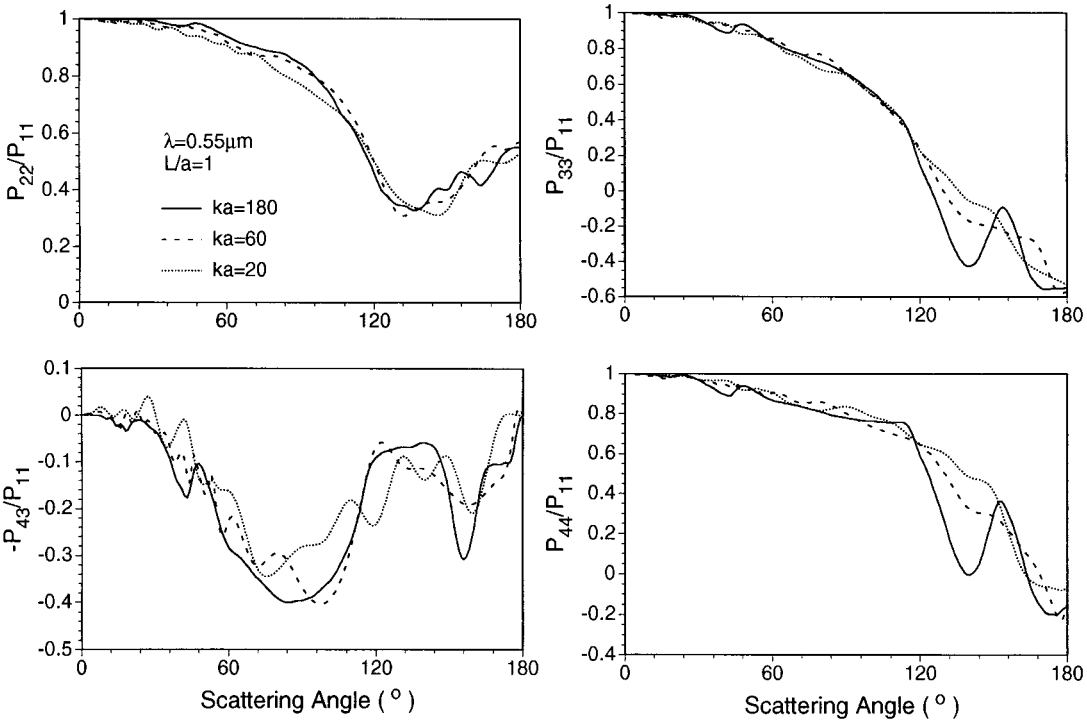

Fig. 9. Remaining nonzero elements of the phase matrix associated with the results presented in Fig. 8.

because absorption of the transmitted rays increases with the ray path length inside the ice crystals. For the degree of linear polarization, the results fluctuate greatly for small size parameters associated with the significant phase interferences. The polarization configuration of the scattered field is more sensitive to the phase interferences than the scattered intensity.

Figure 9 shows the remaining nonzero phase matrix elements at the 0.55-μm wavelength. For P_{22}/P_{11}, differences are small for the three size parameters. For $-P_{43}/P_{11}$, the fluctuation decreases for an increasing size parameter because the phase interference effect is largely averaged out. For P_{33}/P_{11} and P_{44}/P_{11}, we find that differences for the three size parameters are mainly in the scattering angle region of 120–180°. The results for the absorbing wavelength ($\lambda = 3.7$ μm) not shown here vary greatly with size parameters, similar to the linear polarization pattern. In summary, the polarization configuration of light scattering by ice crystals is more sensitive to the size parameter at the absorbing wavelength than at the visible wavelength.

Comparisons of the phase functions computed by GOM2 with those by the exact FDTD method that we developed[5] are presented in Fig. 10 for $kL = 20$ with two aspect ratios: $(L/a = 6)$ and $(L/a = 2)$. For the former, the ice crystal cross section is too small, so the localization principle for the computation of surface fields may not be applicable. Large deviations are noted, particularly when the scattering angle is larger than 70°, where the contribution from higher-order terms in the multipole expansion of the scattered field is significant. For the latter, because the ice crystal cross section is increased by a factor of 3, the accuracy of GOM2 is greatly improved and the computed major features mimic those produced by the FDTD method. In terms of the extinction cross section illustrated in Fig. 4, the GOM2 values approach the FDTD results when $kL \rightarrow 20$, revealing that GOM2 is an excellent method for the calculation of light scattering by ice crystals with size parameters larger than approximately 20, above which the FDTD method becomes extremely expensive computationally with inherent numerical limitations. Also shown in Fig. 10 are the phase functions computed by GOM2 and FDTD for hollow columns and bullet rosettes. The depth of the hollow pyramid is indicated by d; the cross angle for the bullets is 90°, the tip length of a bullet is t; and other parameters defining the geometry of the ice crystals are given in the diagrams. The scattering patterns for solid and hollow column crystals are similar, except in the backscattering directions. In particular, a pronounced scattering maximum is shown at the scattering angle of ~155° in both cases. However, this feature does not appear in the case of bullet rosettes.

5. Conclusions

Motivated by quantifying the scattering and absorption characteristics of small ice crystals, for which the conventional geometric ray-tracing technique breaks down, we have extended our geometric-optics–integral-equation hybrid method for the 2-D case to the computation of the complete Stokes phase matrix, extinction efficiency, and single-scattering albedo for ice crystals in 3-D space. In the improved method we used the geometric ray-tracing procedure to solve

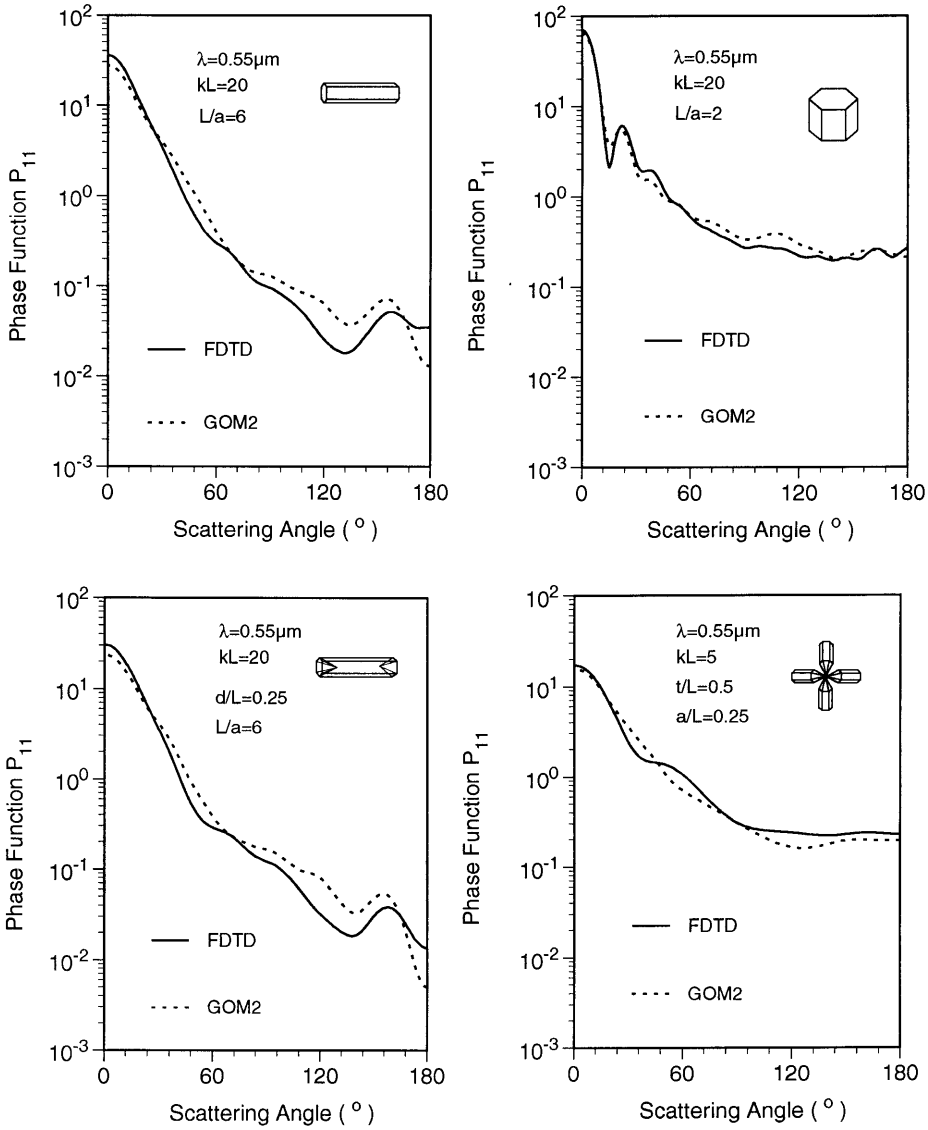

Fig. 10. Comparison of the phase functions computed by GOM2 and the FDTD method at the 0.55-μm wavelength for solid and hollow columns, plates, and bullet rosettes.

the near field on the particle surface, which was then transformed to the far field on the basis of the electromagnetic equivalence theorem. To economize the computational effort, we developed an efficient intensity mapping algorithm in which the conventional geometric ray-tracing program for reflection and refraction can be employed in the calculations directly.

We find that the phase interference and the vector property of various localized waves must be taken into account for size parameters less than ~ 20 and 30. For size parameters larger than ~30 but smaller than ~200, the phase interference between various transmitted and externally reflected rays can be neglected. However, the spreading of the rays caused by their finite cross sections must be accounted for.

We show that the present geometric-optics–integral-equation hybrid method is applicable to the computation of extinction and scattering cross sections when the size parameter along the minimum dimension is larger than ~6. With verification from the FDTD results, we find that it can also be applied to compute reliably the phase functions if the size parameter is larger than ~20. We demonstrate that the present model converges to the conventional ray-tracing method for large size parameters and produces single-scattering results close to the FDTD results for small size parameters. It is concluded that the present method can bridge the gap of the applicable regions of size parameters associated with the conventional ray-tracing and accurate numerical methods.

Appendix A

The matrices associated with the geometric transformation and the rotation of coordinate systems pre-

sented in the text are defined as follows:

$$\Lambda_p = \begin{cases} \begin{bmatrix} \hat{\beta}_1 \cdot \hat{\beta}^i & -\hat{\beta}_1 \cdot \hat{\alpha}^i \\ \hat{\beta}_1 \cdot \hat{\alpha}^i & \hat{\beta}_1 \cdot \hat{\beta}^i \end{bmatrix} & \text{for } p = 1 \\ \begin{bmatrix} \hat{\beta}_p \cdot \hat{\beta}_{p-1} & -\hat{\beta}_p \cdot \hat{\alpha}_{p-1} \\ \hat{\beta}_p \cdot \hat{\alpha}_{p-1} & \hat{\beta}_p \cdot \hat{\beta}_{p-1} \end{bmatrix} & \text{for } p \geq 2 \end{cases}, \tag{A1}$$

$$\mathbf{K}_p = \begin{bmatrix} \hat{\alpha}^s \cdot \hat{\nu}_p & \hat{\alpha}^s \cdot \hat{\mu}_p \\ \hat{\beta}^s \cdot \hat{\nu}_p & \hat{\beta}^s \cdot \hat{\mu}_p \end{bmatrix}, \qquad \tilde{\mathbf{K}}_p = \begin{bmatrix} \hat{\alpha}^s \cdot \hat{\eta}_p & \hat{\alpha}^s \cdot \hat{\xi}_p \\ \hat{\beta}^s \cdot \hat{\eta}_p & \hat{\beta}^s \cdot \hat{\xi}_p \end{bmatrix}. \tag{A2}$$

$$\mathbf{Y}_p{}^s = \begin{bmatrix} \hat{\nu}_p \cdot \hat{\alpha}_p{}^s & \hat{\nu}_p \cdot \hat{\beta}_p \\ \hat{\mu}_p \cdot \hat{\alpha}_p{}^s & \hat{\mu}_p \cdot \hat{\beta}_p \end{bmatrix}, \qquad \tilde{\mathbf{Y}}_p{}^s = \begin{bmatrix} \hat{\eta}_p \cdot \hat{\alpha}_p{}^s & \hat{\eta}_p \cdot \hat{\beta}_p \\ \hat{\xi}_p \cdot \hat{\alpha}_p{}^s & \hat{\xi}_p \cdot \hat{\beta}_p \end{bmatrix}. \tag{A3}$$

$$\mathbf{Y}_1 = \begin{bmatrix} \hat{\nu}_1 \cdot \hat{\alpha}_1 & \hat{\nu}_1 \cdot \hat{\beta}_1 \\ \hat{\mu}_1 \cdot \hat{\alpha}_1 & \hat{\mu}_1 \cdot \hat{\beta}_1 \end{bmatrix}, \qquad \mathbf{J} = \begin{bmatrix} 0 & 1 \\ -1 & 0 \end{bmatrix}. \tag{A4}$$

$$\Pi_1 = \begin{bmatrix} \hat{\alpha}^s \cdot \hat{\alpha}_1 & \hat{\alpha}^s \cdot \hat{\beta}_1 \\ \hat{\beta}^s \cdot \hat{\alpha}_1 & \hat{\beta}^s \cdot \hat{\beta}_1 \end{bmatrix}, \qquad \Pi_2{}^s = \begin{bmatrix} \hat{\alpha}^s \cdot \hat{\alpha}_2{}^s & \hat{\alpha}^s \cdot \hat{\beta}_2 \\ \hat{\beta}^s \cdot \hat{\alpha}_2{}^s & \hat{\beta}^s \cdot \hat{\beta}_2 \end{bmatrix} \tag{A5}$$

$$\Gamma^i = \begin{bmatrix} \hat{\beta}^s \cdot \hat{\beta}^i & \hat{\beta}^s \cdot \hat{\alpha}^i \\ -\hat{\beta}^s \cdot \hat{\alpha}^i & \hat{\beta}^s \cdot \hat{\beta}^i \end{bmatrix}, \qquad \tilde{\Gamma}_p{}^i = \begin{bmatrix} \hat{\xi}_p \cdot \hat{\beta}^i & \hat{\xi}_p \cdot \hat{\alpha}^i \\ -\hat{\xi}_p \cdot \hat{\alpha}^i & \hat{\xi}_p \cdot \hat{\beta}^i \end{bmatrix}. \tag{A6}$$

$$\Gamma_p{}^s = \begin{bmatrix} \hat{\xi}_p \cdot \hat{\beta}^s & -\hat{\xi}_p \cdot (\hat{e}^i \times \hat{\beta}^s) \\ \hat{\xi}_p \cdot (\hat{e}^i \times \hat{\beta}^s) & \hat{\xi}_p \cdot \hat{\beta}^s \end{bmatrix}. \tag{A7}$$

$$\Xi = \begin{bmatrix} \cos\theta \cos\theta_t \cos\varphi_t + \sin\theta \sin\theta_t & -\cos\theta \sin\varphi_t \\ \cos\theta_t \sin\varphi_t & \cos\varphi_t \end{bmatrix}. \tag{A8}$$

In the preceding equations, the unit vectors defining the directions are given in the text and in Figs. 1 and 3.

Appendix B

To illustrate the concept of spreading, let us consider the far field contributed from a transmitted ray shown in Fig. 7. For simplicity but without loss of generality, we assume that both the particle and the transmitted ray are unbounded in the y direction (perpendicular to the paper). However, the localized wave is finite in the x direction and confined to the region of $(-l, l)$. In GOM1, the transmitted ray will contribute to the far field only in the direction determined by Snell's law. This, however, is the asymptotic solution for a unbounded plane wave. Using Eqs. (36) and (38), we can obtain the amplitude scattering matrix contributed by the outgoing ray with the order $p = 2$ as follows:

$$\mathbf{S}_{p=2} = -\frac{k^2}{4\pi} \exp[i(\delta_0 - \hat{r} \cdot \mathbf{r}_{Q_2})](\hat{n}_{s,2} \cdot \hat{r} + \hat{n}_{s,2} \cdot \hat{e}_2{}^s)\Pi_2{}^s \mathbf{T}_2 \mathbf{T}_1 \Gamma^i \kappa_x \kappa_y, \tag{B1}$$

where $\Pi_2{}^s$ is defined in Appendix A; $\mathbf{T}_1$ and $\mathbf{T}_2$ are Fresnel transmission matrices as given by Eq. (13g); δ_0 is the phase of the outgoing localized wave at point Q_2; and

$$\kappa_y = \int_{-\infty}^{\infty} \exp(-ikr_y y)\mathrm{d}y = \frac{2\pi}{k}\,\delta(r_y), \tag{B2a}$$

$$\kappa_x = \int_{-l}^{l} \exp[ik(e_{2,x}{}^s - r_x)x]\mathrm{d}x = 2l\,\frac{\sin[kl(\sin\varphi - \sin\varphi_t)]}{kl(\sin\varphi - \sin\varphi_t)}, \tag{B2b}$$

where $\mathrm{r_x}$ and r_y are the x and y components of $\hat{r}$, respectively; $e_{2,x}{}^s$ is the x component of $\hat{e}_2{}^s$; and φ and φ_t are the angles defined in Fig. 7(a). Therefore, the scattered field can be observed only in the directions confined to the x–y plane, that is, $r_y = 0$. If the incident field is polarized in the y direction, the angular distribution of the scattered field contributed by the outgoing ray is given by

$$E(\varphi - \varphi_t) = (\hat{n}_{s,2} \cdot \hat{r} + \hat{n}_{s,2} \cdot \hat{e}_2{}^s)\kappa_x = (\cos\varphi + \cos\varphi_t)\kappa_x. \tag{B3}$$

Consequently, the normalized angular distribution for the scattered intensity is given by

$$I(\varphi, \varphi_t) = |E(\varphi, \varphi_t)|^2/c', \tag{B4}$$

where c' is a normalization constant. Figure 7(b) shows the pattern of $I(\varphi, \varphi_t)$ for $\varphi_t = 0°$ and $45°$. First, it can be seen that the contribution of the outgoing ray to the far field is global and no longer local as in GOM1. When kl increases, more scattered energy will concentrate in the direction predicted by Snell's law. Second, the number of the side-scattering lobes with respect to the direction of $\hat{e}_2{}^s$ increases with the increase of the ray width. Finally, $I(\varphi, \varphi_t) \to (2\pi)^{-1}\delta(\varphi - \varphi_t)$ when $kl \to \infty$. In the 3-D case that involves scattering by hexagonal ice crystals, we find that the spreading effect for the transmitted rays can be neglected when the characteristic size parameters are larger than ~100.

This study was supported by the National Science Foundation under grant ATM-93-1521, in part by NASA grants NAG1-1719 and NAG5-2678, and by the U.S. Department of Energy under grant DE-FG03-95ER61991. Most of the computational results presented here were obtained from the use of CRAY Y-MP 8/864 at the National Center for Atmospheric Research, sponsored by the National Science Foundation.

References

1. A. J. Heymsfield, "Cirrus uncinus generating cells and the evolution of cirriform clouds. Part I: Aircraft observations of the growth of the ice phase," J. Atmos. Sci. **32,** 799–808 (1975).
2. A. J. Heymsfield, K. M. Miller, and J. D. Sphinhirne, "The 27–28 October 1986 FIRE IFO cirrus case study: cloud microstructure," Mon. Weather Rev. **118,** 2313–2328 (1990).
3. L. M. Miloshevich, A. J. Heymsfied, and P. M. Norris, "Microphysical measurements in cirrus clouds from ice crystals replicator sonders launched during FIRE II," in *Proceedings of the*

11th International Conference on Clouds and Precipitation (17–21 August 1992), Vol. 1, pp. 525–528.
4. A. Taflove, *Computational Electrodynamics: The Finite-Difference Time Domain Method* (Artech, Boston, 1995).
5. P. Yang and K. N. Liou, "Light scattering by hexagonal ice crystals: comparison of finite-difference time domain and geometric optics models," J. Opt. Soc. Am. A **12,** 162–176 (1995).
6. P. Yang and K. N. Liou, "Finite-difference time domain method for light scattering by small ice crystals in three-dimensional space," J. Opt. Soc. Am. A **13,** 2072–2085 (1996).
7. E. M. Purcell and C. P. Pennypacker, "Scattering and absorption of light by nonspherical dielectric grains," Astrophys. J. **186,** 705–714 (1973).
8. B. T. Draine and P. J. Flatau, "Discrete-dipole approximation for calculations," J. Opt. Soc. Am. A **11,** 1491–1499 (1994).
9. K. N. Liou and Y. Takano, "Light scattering by nonspherical particles: remote sensing and climatic implications," Atmos. Res. **31,** 271–298 (1994).
10. Q. Cai and K. N. Liou, "Polarized light scattering by hexagonal ice crystals: theory," Appl. Opt. **21,** 3569–3580 (1982).
11. Y. Takano and K. N. Liou, "Solar radiation transfer in cirrus clouds. Part I: Single-scattering and optical properties of hexagonal ice crystals," J. Atmos. Sci. **46,** 3–19 (1989).
12. Y. Takano and K. N. Liou, "Radiative transfer in cirrus clouds. Part III: Light scattering by irregular ice crystals," J. Atmos. Sci. **52,** 818–837 (1995).
13. K. Muinonen, "Scattering of light by crystals: a modified Kirchhoff approximation," Appl. Opt. **28,** 3044–3050 (1989).
14. A. Macke, "Scattering of light by polyhedral ice crystals," Appl. Opt. **32,** 2780–2788 (1993).
15. S. A. Schelkunoff, *Electromagnetic Waves* (Van Nostrand, New York, 1943).
16. B. Karczewski and E. Wolf, "Comparison of three theories of electromagnetic diffraction at an aperture. Part I: Coherence matrices," J. Opt. Soc. Am. **56,** 1207–1214 (1966).
17. H. C. van de Hulst, *Light Scattering by Small Particles* (Wiley, New York, 1957).
18. J. I. Hage, J. M. Greenberg, and R. T. Wang, "Scattering from arbitrarily shaped particles: theory and experiment," Appl. Opt. **30,** 1141–1152 (1991).
19. C. T. Tai, *Dyadic Green's Function in Electromagnetic Theory* (International Textbook, Scranton, 1971), Chap. 4, pp. 48–49.
20. E. Wolf, "A generalized extinction theorem and its role in scattering theory," in *Coherence and Quantum Optics*, L. Mandel and E. Wolf, eds. (Plenum, New York, 1973), pp. 339–359.
21. C. W. Oseen, "Uber die Wechselwirkung zwischen zwei elektrichen Dipolen und uber die Drenhung der Polarisationsebene in Kristallen und Flussigkeiten," Ann. Phys. **48,** 1–15 (1915).
22. K. N. Liou and J. E. Hansen, "Intensity and polarization for single scattering by polydisperse spheres: a comparison of ray optics and Mie theory," J. Atmos. Sci. **28,** 995–1004 (1971).
23. Y. Takano and M. Tanaka, "Phase matrix and cross sections for single scattering by circular cylinders: a comparison of ray optics and wave theory," Appl. Opt. **19,** 2781–2793 (1980).
24. A. Macke, M. I. Mishchenko, K. Muinonen, and B. E. Carlson, "Scattering of light by large nonspherical particles: ray-tracing approximation versus T-matrix method," Opt. Lett. **20,** 1934–1936 (1995).
25. J. A. Lock, "Ray scattering by an arbitrarily oriented spheroid. I. Diffraction and specular reflection," Appl. Opt. **35,** 500–514 (1996); "II. Transmission and cross-polarization effects," Appl. Opt. **35,** 515–531 (1996).